

Neuron, Volume 99

Supplemental Information

**Linking Connectivity, Dynamics,
and Computations in Low-Rank
Recurrent Neural Networks**

Francesca Mastrogiuseppe and Srdjan Ostojic

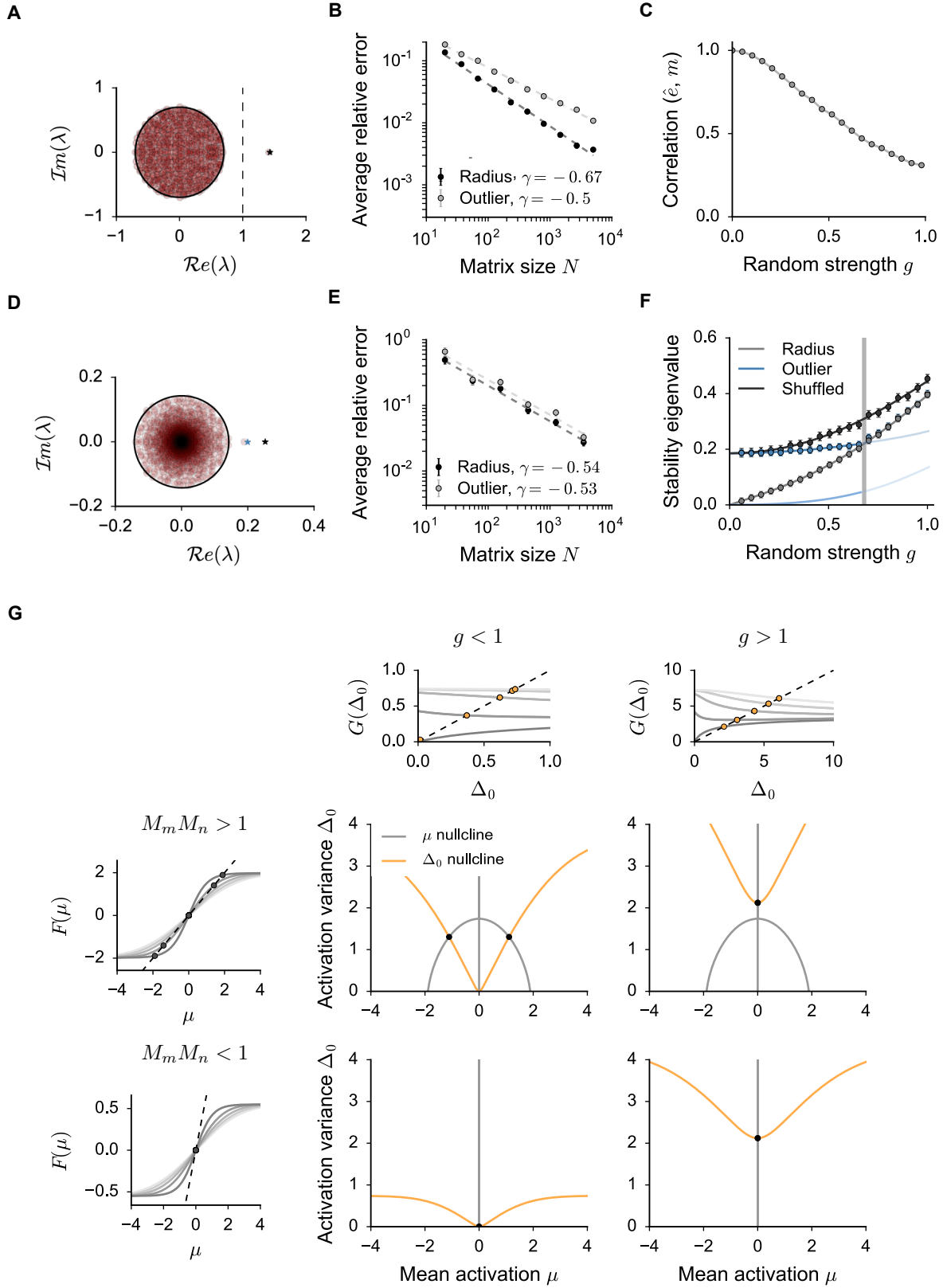


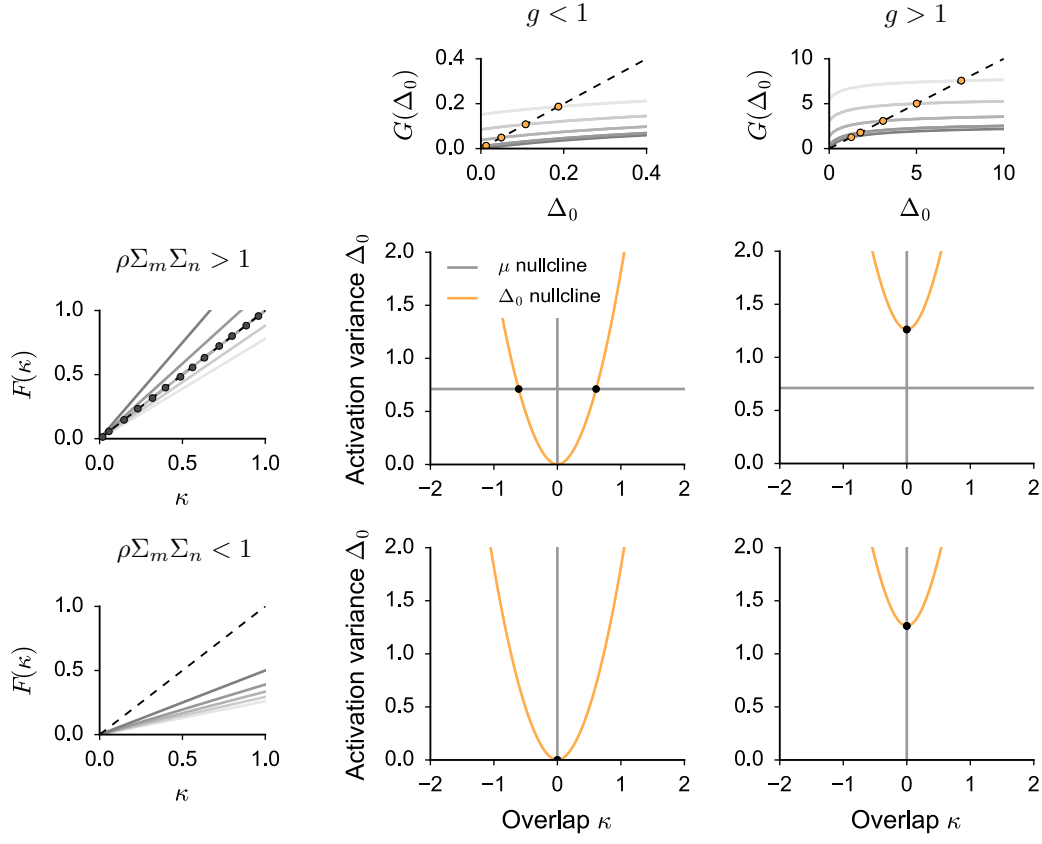
Figure S1 (*previous page*): **Dynamical Mean-Field description of rank-one networks whose right- and left-connectivity vectors overlap solely on the unitary direction** ($\rho = 0$, see *Methods*). Related to Figure 1.

(A-B-C) Eigenspectrum of the partially structured connectivity matrix J_{ij} , related to the stability matrix S_{ij} of the homogeneous fixed points through: $S_{ij} = \phi'(\bar{x})J_{ij}$. **A.** Eigenspectrum of J_{ij} in the complex plane. Red dots: eigenspectrum of a single realization J_{ij} of size $N = 1000$. In black: theoretical prediction. Every matrix J_{ij} consists of a sum of a random and of a fixed unit-rank structure. In the large N limit, the spectrum of the full matrix is given by the sum of the eigenspectra of the two parts. The black circle has radius equal to the total random strength g , and the black star indicates the position of the non-zero eigenvalue of the rank-one structure P_{ij} . **B.** Mismatch between the statistics measured in finite-size networks (x_{sim}) and the theoretical prediction (x_{th}) as the network size N is increased. The error is normalized: $|x_{sim} - x_{th}|/x_{th}$. Averages over 100 realizations. The error bars (as in every other figure, if not differently specified) correspond to the standard deviation of the mean. Dashed lines: power-law best fit ($y \propto N^\gamma$). The values of γ are indicated in the legend. **C.** Pearson correlation coefficient between the connectivity eigenvector m and the eigenvector \hat{e} which corresponds to the outlier eigenvalue. Choice of the parameters: $\rho = 0$, $M_m M_n = 1.43$, $\Sigma_m = 0.33$, $\Sigma_n = 1$. In A and B, $g = 0.7$.

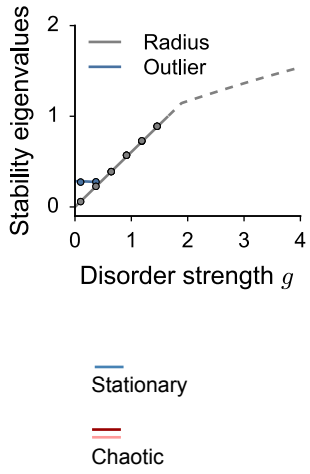
(D-E-F) Analysis of the eigenspectrum of the linear stability matrix $S_{ij} = \phi'(\bar{x})J_{ij}$ for heterogeneous stationary solutions. **D.** Eigenspectrum of S_{ij} in the complex plane. Red dots: eigenspectrum of a single, finite-size realization of S_{ij} , $N = 2500$. The radius of the black circle corresponds to the theoretical prediction $r = g\sqrt{\langle[\phi_i'^2]\rangle}$. The black star indicates the position of the non-zero eigenvalue of the rank-one structure $m_i\phi'(x_j^0)n_j/N$, which deviates significantly from the position of the outlier eigenvalue. We thus address the problem of evaluating the position of the outlier eigenvalue through a mean-field stability analysis (Eq. 71), the prediction of which is indicated by the blue star. **E.** Mismatch between the results from simulations and mean-field predictions for the radius and the outlier position. The error is measured as an average over $N_{tr} = 30$ finite size matrices, and decays as the system size is increased. Details as in B. **F.** Radius and outlier of the stability eigenspectrum for increasing random strength values. The dots indicate the results of numerical simulations of networks with $N = 2500$ units, averaged over $N_{tr} = 30$ realizations of the random and structured connectivities. In grey: radius of the compact bulk (continuous line: mean-field prediction r). In blue: position of the outlier eigenvalue (continuous dark and light lines: first and second eigenvalue of matrix \mathcal{M} given in Eq. 71). In black: position of the outlier when χ_{ij} is shuffled (continuous line: mean-field prediction for the outlier of the structured part $m_i\phi'(x_j^0)n_j/N$). Choice of the parameters: $\rho = 0$, $M_m M_n = 2.2$, $\Sigma_m = 0.4$, $\Sigma_n = 1$. In D and E, $g = 0.5$.

(G) Graphical analysis of stationary solutions. Large figures: nullcline plots for the population-averaged DMF equations in Eq. 83. Black dots indicate the solutions that are stable with respect to the outlier eigenvalue. Four set of parameters (two values for $M_m M_n$, two for g) have been selected. Note that the shapes of the μ and the Δ_0 nullcline depend only on the structure strength $M_m M_n$ and the disorder strength g . For the figures in the first (resp. second) row, the structure strength $M_m M_n = 0.55$ (resp. $M_m M_n = 2.0$) is weak (resp. strong). For the figures in the first (resp. second) column: the random strength $g = 0.7$ (resp. $g = 2.0$) is weak (resp. strong). Note that the stationary states at large g values (right column) are always unstable with respect to the continuous component of their stability eigenspectra (Fig. 1 C-D). The small side figures associated to every row and column show how the μ (for the rows) and Δ_0 (for the columns) nullclines have been built. We solve $\mu = F(\mu)$ (resp. $\Delta_0 = G(\Delta_0)$) for different initial values of Δ_0 (resp. μ). Different initial conditions are displayed in gray scale. Dark grey refers to $\Delta_0 = 0$ (resp. $\mu = 0$). The dots indicate the solutions for different initial values, which together generate the nullcline curves. Choice of the parameters: $\Sigma_m = 1$.

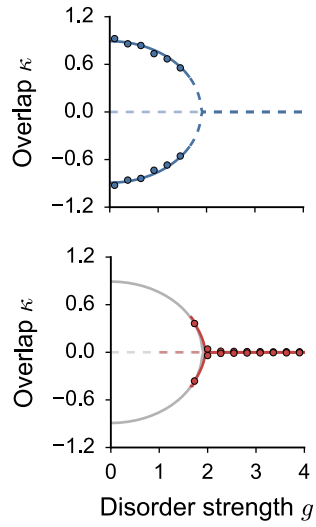
A



B



C



D

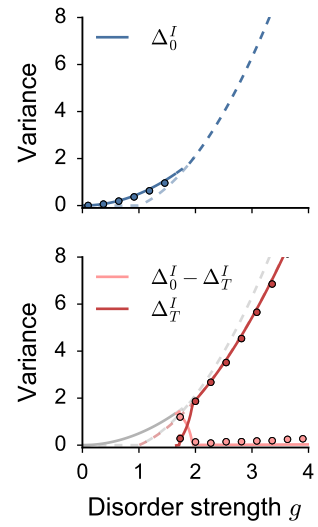


Figure S2 (*previous page*): **Dynamical Mean-Field description of rank-one networks whose right- and left-connectivity vectors overlap onto an arbitrary direction y** ($M_m = M_n = 0$, $\rho \neq 0$, see *Methods*). Related to Figure 1.

(A) Graphical analysis of stationary solutions. Large figures: nullcline plots for the population-averaged DMF equations in Eq. 89. Black dots indicate the solutions that are stable with respect to the outlier eigenvalue. Four set of parameters (two values for $\rho\Sigma_m\Sigma_n$, two for g) have been selected. Note that the shapes of the κ and the Δ_0 nullcline depend only on the structure strength $\rho\Sigma_m\Sigma_n$ and the disorder strength g . For the figures in the first (resp. second) row, the structure strength $\rho\Sigma_m\Sigma_n$ (resp. $\rho\Sigma_m\Sigma_n$) is weak (resp. strong). For the figures in the first (resp. second) column: the random strength $g = 0.5$ (resp. $g = 1.7$) is weak (resp. strong). Note that the stationary states at large g values (right column) are always unstable with respect to the continuous circular component of their stability eigenspectra (see B-C-D). The small figures associated to every row and column show how the κ (for the rows) and Δ_0 (for the columns) nullclines have been built. We solve $\kappa = F(\kappa)$ (resp. $\Delta_0 = G(\Delta_0)$) for different initial values of Δ_0 (resp. κ). Different initial conditions are displayed in gray scale. Dark grey refers to $\Delta_0 = 0$ (resp. $\kappa = 0$). The dots indicate the solutions for different initial values, which together generate the nullcline curves.

(B-C-D) Bifurcation diagram of the activity statistics as the random strength g is increased. Details as in Fig. 1 C-D. **B.** Stability eigenspectrum of stationary solutions, mean-field prediction for the radius of the compact part and the outlier position. **C.** Overlap $\kappa = \langle n_i[\phi_i] \rangle$. **D.** Individual second order statistics. The DMF solutions are displayed as continuous (resp. dashed) lines if they correspond to a stable (resp. unstable) state. In C-D, top panels display statistics for stationary solutions and bottom panels display statistics for chaotic solutions. Dots: we measured activity statistics in finite-size networks, starting from globally positive and negative initial conditions. Activity is integrated up to $T = 400$. $N = 3500$, average over 8 different network realizations. Choice of the parameters: $\Sigma_m = \Sigma_n = 1.5$, $\rho = 2.0/\Sigma_m\Sigma_n$.

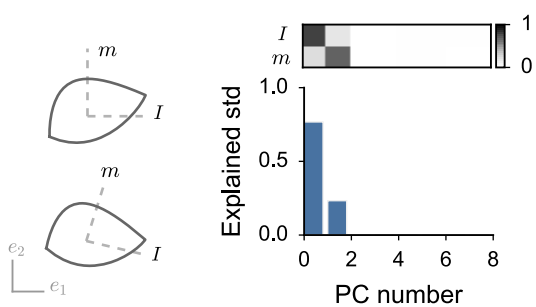
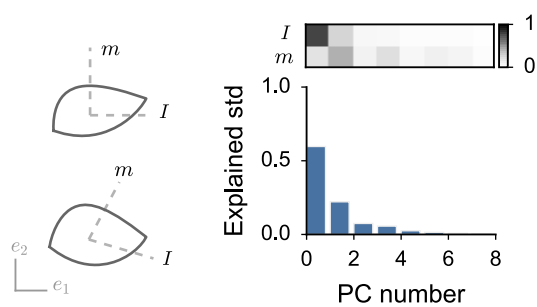
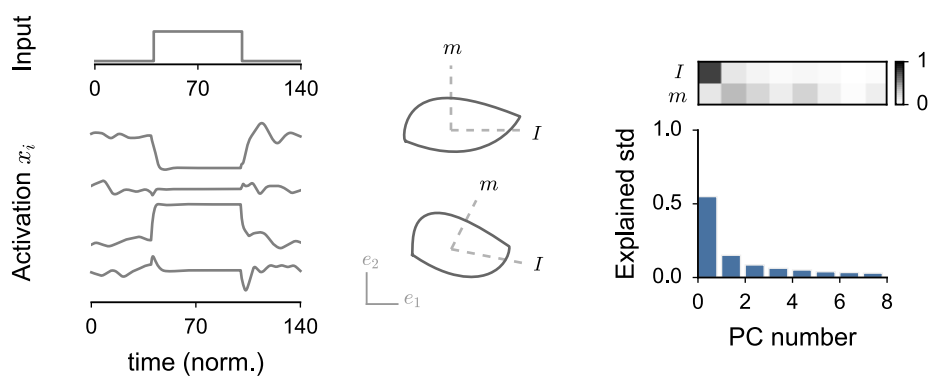
A**B****C**

Figure S3: **Two-dimensional dynamics in networks with unit-rank structure and external inputs.** Related to Figure 2.

We consider a unit-rank network as in Fig. 2 B-C. The connectivity vectors m and n are orthogonal, but the external input vector contains a component along n , whose strength (quantified by Σ_{nI} , see *Methods*) undergoes a step increase from 0.2 to 2.0. We simulate data from networks of size $N = 3500$. We analyze the dimensionality of the dynamics by comparing the relevant low-dimensional trajectory predicted by the mean-field theory with the strongest modes extracted through dimensionality reduction (Principal Component analysis, see *Methods*).

A. Analysis for a purely structured network ($g = 0$). Left top: the mean-field theory predicts that the low-dimensional network dynamics $x = \{x_i\}$ lies in the plane defined by the right-connectivity vector m and the external input I . We thus projected the high-dimensional population activity (dark grey trajectory) on this plane. Left bottom: we projected the network dynamics (continuous), along with the two vectors m and I (dashed), on the plane defined by the first two PC axis e_1 and e_2 . Right top: Pearson correlation coefficient between vectors m and I and the first eight PC. Right bottom: strength of the first eight PC, measured as the fraction of the standard deviation of activity that they explain (see *Methods*). Note that when the network connectivity is fully structured ($g = 0$) as in this case, activity is exactly two-dimensional. The first two PC axis span the $m - I$ plane, but they define a rotated set of basis vectors. **B.** Analysis for a network which includes a random term in the connectivity matrix ($g = 0.8$). While in Fig. 2 we performed the PC decomposition on trial-averaged data ($N_{tr} = 20$), here we considered a single trial, defined as a single realization of the random connectivity matrix. Details as in A. Note that the random component of the connectivity adds noisy contributions in a continuum of PC directions, whose strength depends on the value of g with respect to the amplitude of input and connectivity vectors, and becomes weaker and weaker when averaging with respect to different realizations of χ_{ij} . When $g > 0$, vectors m and I are not fully contained in the $e_1 - e_2$ plane, so their projections on the PC plane are not orthogonal. **C.** Analysis for a network which includes a strong random term in the connectivity matrix ($g = 1.8$), such that spontaneous activity is chaotic. In the left-most column, similarly to Fig. 2, we plot the time trajectories of four randomly selected units. The center and the right columns are as in A and B, with PCA performed on trial-averaged activity ($N_{tr} = 20$). The scale of the projections panels is here set arbitrarily.

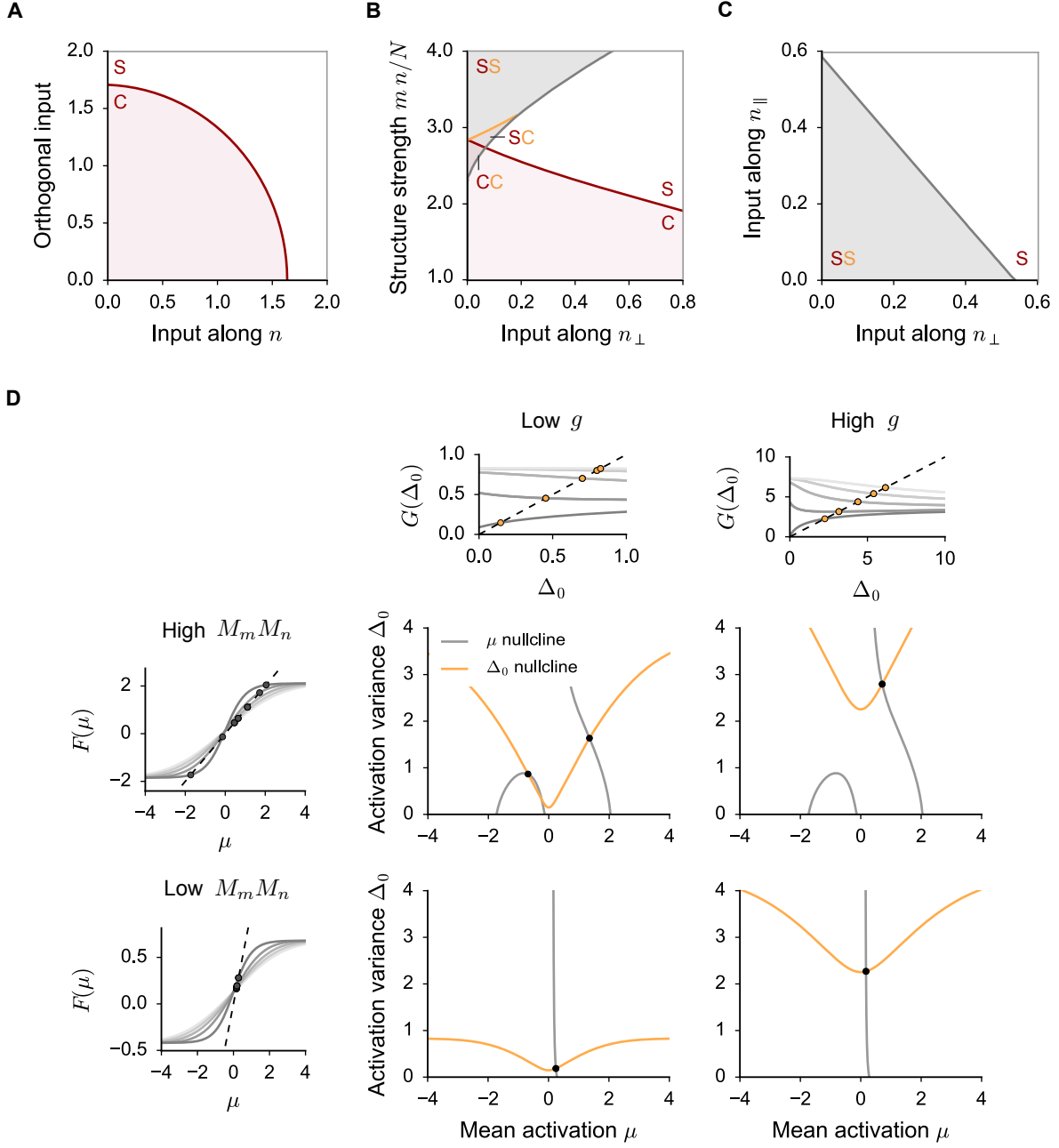


Figure S4 (*previous page*): **Dynamical Mean-Field description of input-driven dynamics for rank-one networks whose right- and left-connectivity vectors overlap solely on the unitary direction** ($\rho = 0$, see *Methods*). Related to Figure 2.

(A-B-C) Dynamical regimes of the network activity as function of the structure connectivity strength $m^T n/N$, the random strength g and the input strength. Grey shaded areas indicate the parameter regions where the network activity is bistable. Red shaded areas indicate the phase space regions where network dynamics are chaotic. When two stable solutions exist, the yellow and the red letter indicate whether each of them is stationary (S) or chaotic (C). Note that stationary and chaotic dynamics can coexist (SC region). In **A**, as in Fig. 2 D center, the two connectivity vectors m and n are orthogonal. We varied the external input strength by increasing the amplitude of the component along n (quantified by Σ_{nI} , see *Methods*) and of the orthogonal one (quantified by Σ_{\perp}). Note that inputs along both directions contribute to suppressing the amplitude of chaotic fluctuations. In **B**, as in Fig. 2 D right, the two connectivity vectors m and n are not orthogonal, but they share an overlap component along the unitary direction. We varied the structure strength (quantified by $M_m M_n$) and the strength of the input along the direction of n that is perpendicular to the structure overlap, n_{\perp} (again quantified by Σ_{nI}). Similarly to Fig. 1, strong structure overlaps can lead to the appearance of two bistable solutions. In presence of non trivial external inputs, however, such solutions are not symmetric, and can loose stability on different parameter boundaries. In particular, we observe that external inputs tend to suppress bistable regimes, by favouring one solution over the other. In **C**, finally, the network configuration is similar to B, but we consider external inputs which include a second component along the direction of n that is shared with m , n_{\parallel} (quantified by M_I). We observe that both input directions play similar roles in reducing the extent of the bistable regime. Choice of parameters: $g = 2.2$, $\Sigma_m = \Sigma_n = 1.0$, $\Sigma_{mI} = 0$.

(D) Graphical analysis of stationary solutions. In this example, the external input vector overlaps with n on the unitary overlap direction n_{\parallel} ($M_I = 0.13$), and includes orthogonal components quantified by $\Sigma_I = 0.3$. Large figures: nullcline plots for the stationary form of the population-averaged DMF equations in Eq. 98. Black dots indicate the solutions that are stable with respect to the outlier eigenvalue. Four set of parameters (two values for $M_m M_n$, two for g) have been selected. Note that the shape of the μ and the Δ_0 nullcline depends only, respectively, on the structure strength $M_m M_n$ and the disorder g together with the input statistics. For the figures in the first (resp. second) row, the structure strength $M_m M_n = 0.55$ (resp. $M_m M_n = 2.0$) is weak (resp. strong). For the figures in the first (resp. second) column: the random strength $g = 0.7$ (resp. $g = 2.0$) is weak (resp. strong). The small figures associated to every row and column show how the μ (for the rows) and Δ_0 (for the columns) nullclines have been built. We solve $\mu = F(\mu)$ (resp. $\Delta_0 = G(\Delta_0)$) for different initial values of Δ_0 (resp. μ). Different initial conditions are displayed in gray scale. Dark grey refers to $\Delta_0 = 0$ (resp. $\mu = 0$). The dots indicate the solutions for different initial values, which together generate the nullcline curves. Choice of the parameters: $\Sigma_m = 1$.

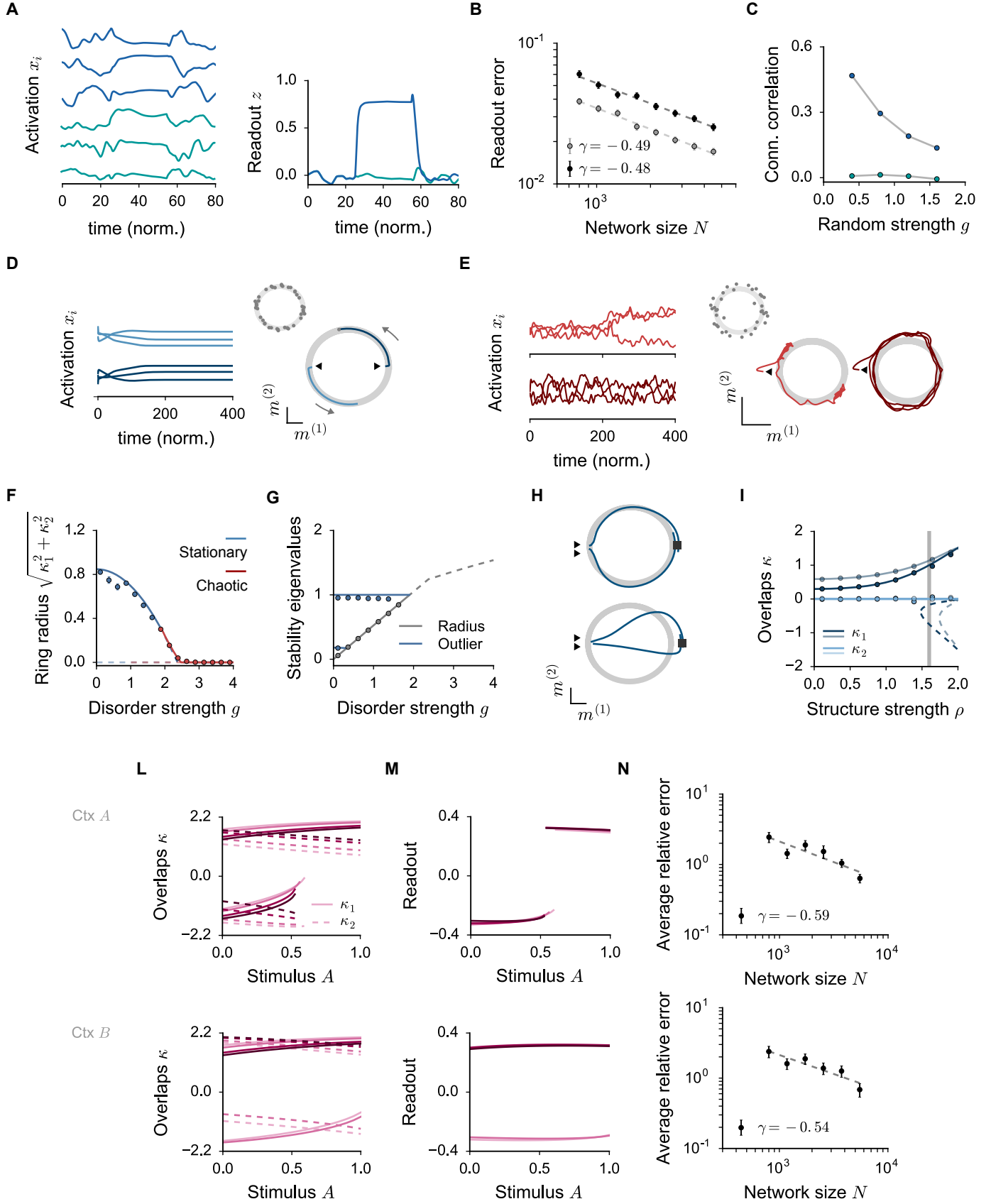


Figure S5 (*previous page*): **Dynamical Mean-Field description of low-rank networks designed for solving computational tasks.** Related to Figures 3, 5 and 6.

(A-B-C) Rank-one networks can robustly perform computations also when their dynamics is chaotic due to large random connectivities. Here, we show an example from the Go-Nogo task (Fig. 3). We focus on large random strength values ($g = 2.5$), so that spontaneous network dynamics is chaotic. **A.** Left: response of three randomly selected units to the Go pattern I^A (top, blue) and to the Nogo pattern I^B (bottom, green). Right: time trace of the readout $z(t)$ for the Go (blue) and the Nogo (green) stimulus. **B.** Absolute, normalized distance between the theoretical prediction and the value of the readout z obtained from finite-size realizations. As expected, the magnitude of the average normalized error decays with the network size as $\sim 1/\sqrt{N}$. In grey: $g = 0.8$, in black: $g = 2.5$. Averages over 200 network realizations. Details as in Fig. S1 B. **C.** As in Fig. 3 F, we consider pairs of units and we compute the correlation coefficient between their weights onto the first PC axis and their average reciprocal connectivity strength. The PC axis is computed separately for data corresponding to Go (blue) or the Nogo (green) trials. The correlation coefficient for the Go trials decreases with the amplitude of the random connectivity, although the error in the readout is only weakly affected (panel **B.**). For every entry of the connectivity matrix J_{ij} , indeed, the random part $g\chi_{ij}$ has larger amplitude than the structured one P_{ij} . As a consequence, the random noise can hide a fraction of the strong correlations existing between the PC weights and the rank-one connectivity P_{ij} . Note that the absolute value of the correlation coefficient depends on the variance of the rank-one connectivity. Finally, the correlation coefficient increases as the connectivity gets averaged on more and more realizations of the random part. Choice of the parameters as in Fig. 3.

(D-E-F-G-H-I) Ring attractor from rank-two connectivity structures with connectivity vectors characterized by strong internal overlaps (see *Methods*). **D.** Sample of activity from a finite-size realization ($N = 4000$) of the rank-two network. Activity is initialized in two different initial conditions (light and dark blue), indicated by the small arrows. Left: time traces of the activation variables for three randomly selected network units. Note the long time range on the x axis. Right: population activation $x = \{x_i\}$ projected on the plane spanned by the right vectors $m^{(1)}$ and $m^{(2)}$. The ring attractor predicted by the mean-field theory is displayed in light gray. The strength of the disorder is $g = 0.5$, so that the network is in a stationary regime. In the small inset, we reproduce the theoretical prediction together with the final state of additional $N_{tr} = 20$ networks realizations, that are displayed as grey dots. **E.** Sample of activity for two finite-size realizations ($N = 4000$) of the structured connectivity matrix (dark and light red). Details as in **D.** The strength of random connections is $g = 2.1$, so that the network is in a chaotic regime. Chaotic fluctuations can occur together with a slow exploration of the ring (dark red). If two specific states on the ring appear to be more stable, chaotic fluctuations can induce jumps between the two of them (light red). **F-G.** Mean-field characterization of the ring structure: radius of the ring attractor and stability eigenvalues. Details as in Fig. 1. Dots: numerical results from finite-size ($N = 4000$) networks, averaged over 6 realizations of the connectivity matrix. **H-I.** Input patterns which correlate with the left vector $n^{(1)}$ reduce the ring attractor to a single stable state. Activity is thus projected in the direction spanned by the right vector $m^{(1)}$. In **H**, we show the input response for two finite-size networks. The grey ring displays the mean-field solution in absence of external inputs ($g = 0.5$, as in **D**). In the top panel, the input is weak ($\Sigma_I = 0.2$, see *Methods*). The transient dynamics as well as the equilibrium state lie close to the ring structure. In the bottom panel, the input is strong ($\Sigma_I = 0.6$), and the ring structure is not anymore clearly apparent. In **I**, we plot the values of the overlaps κ_1 (blue) and κ_2 (azure) as a function of the structure strength parameter ρ , for fixed input strength. Stable solutions are plotted as continuous lines, unstable ones as dashed. Solid (resp. transparent) lines refer to weak (resp. strong) external inputs: $\Sigma_I = 0.2$ (resp. 0.6). The vertical gray line indicate the value of ρ that has been used in **H**. Dots: numerical results as in **F-G**. Choice of the parameters (see *Methods*): $\Sigma = 2.0$, $\rho_1 = \rho_2 = 1.6$.

(L-M-N) Rank-two structures for implementing non-linear stimuli detection in a context-dependent fashion (Fig. 6): theoretical mean-field predictions. **L.** Values of the first-order statistics κ_1 (continuous) and κ_2 (dashed) as a function of the overlap strength along the stimulus I^A . Results are shown for four increasing values of the overlap strength along the second stimulus I^B . Top (resp. bottom): the contextual gating inputs are such that a response to I^A (resp. I^B) is selected. **M.** Readout value, built by summing the values of κ_1 and κ_2 (Eq. 158). Note that although κ_1 and κ_2 vary with input strength, on each branch their sum is approximately constant. Details as in **L**. **N.** Average normalized error between the DMF predictions and the simulated readout, in the two gating conditions as a function of the network size N . Average over 60 network realizations, details as in Fig. S1 B. Parameters as in Fig. 6.

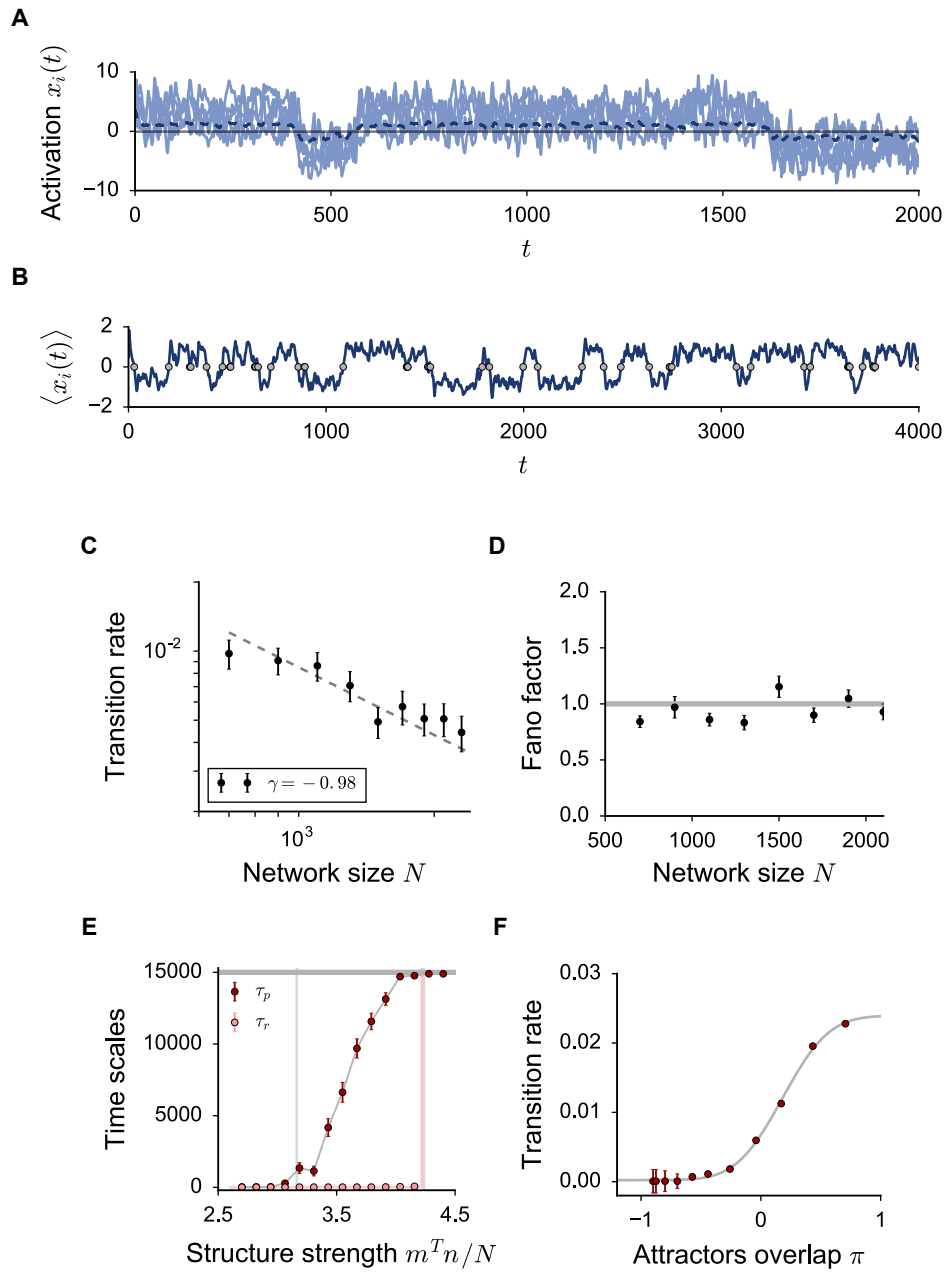


Figure S6 (*previous page*): **Dynamics of unit-rank networks of finite-size are characterized by two distinct time-scales.** Related to Figure 1.

In Fig. 1 we have shown that, when the structure strength is large, the DMF theory predicts the existence of two bistable states, which can display chaotic activity. For those states, the population-averaged statistics of the activation variable x_i are stationary. In the chaotic regime, indeed, irregular temporal fluctuations are decorrelated from one unit to the other, so that the central limit theorem applies at every time step, and the network statistics are constant in time. In finite-size networks, however, the network statistics are not stationary: their dynamics display instead two different time-scales. The instantaneous population-averaged activity undergoes small fluctuations of amplitude $\mathcal{O}(1/\sqrt{N})$, whose time-scale is given by the relaxation decay of chaotic activity. Because of bistability, furthermore, the first-order statistics displays also sharp transitions from positive to negative values and viceversa, which are made possible by the self-sustained temporal fluctuations. In the following, we focus on rank-one structures where the overlap direction is defined along the unitary vector. As a consequence, the relevant first-order statistics is simply the population-average of the activation vector μ (see *Methods*). **A.** Sample from a finite-size network: activation time traces for randomly chosen units displaying attractors jumps. Dashed blue line: time-dependent population average. **B.** Time-dependent population average in a longer trial. **C-D.** We consider transition events as point processes, and we measure the average transition rate. We arbitrarily define a transition point as the time step at which the population-averaged activation crosses zero (grey points in B). In **C**, we show that the transition rate decays to zero as the network size N is increased. Details as in Fig. S1 B. Note that the transition rate depends on the amplitude of finite-size fluctuations measured with respect to the average phase space distance between the two attractors. As a consequence, the transition rate depends on the architecture parameters and on the network size, but also varies strongly from one realization of the connectivity matrix to the other. **D.** Fano factor of the point process for different values of the network size N , which noisily oscillates around 1. For every realization of the network, the jumps count is measured in different windows of the total integration time $T = 15,000$. The Fano factor is measured for every realization and then averaged over $N_{tr} = 30$ different networks. **E-F.** Analysis of the two time-scales displayed by the network dynamics. The first time-scale is measured as the relaxation time constant τ_r , which can be derived within the DMF framework by computing the time decay of the full auto-correlation function $\Delta(\tau)$. The persistence time scale, indicated by τ_p , coincides instead with the average time interval which separates two attractors transitions. In **E**, we show that both time scales depend on the network architecture parameters. Here, we fix the random strength $g = 3$ and we increase the structure strength. When the structure is weak (left), the network is in the classical homogeneous chaotic state. The persistence time scale coincides here with the relaxation time constant of chaotic fluctuations. When the structured and the random components have comparable strengths, instead, two heterogeneous chaotic phases co-exist (center). In this regime, the average persistence time increases monotonically with the structure strength, and reaches arbitrarily large values. Note that the relaxation time undergoes a very slow increase before sharply diverging at the boundary with stationary states, but the increase takes place on a much smaller scale. Finally, if the structure is too strong (right), the two bistable states become stationary. In this region, τ_r is formally infinite, while τ_p coincides with the total duration of our simulations. Pink continuous line: DMF prediction, measured as the full width half maximum of the auto-correlation function $\Delta(\tau)$. Pink dots: a rough estimate of τ_r from finite size networks is obtained by rectifying the population average signal and we computing the full width half maximum of its auto-correlation function. **F.** We compare the average transition rate with the average overlap between the two attractors in the phase space. For every unit, the typical overlap between its positive and its negative trajectories is given by $\pi_i = 2(-\mu - \sqrt{\Delta_\infty}z + \sqrt{\Delta_0 - \Delta_\infty})$. We average across the population, yielding: $\pi = 2(-\mu + \sqrt{\Delta_0 - \Delta_\infty})$. We then normalize π through dividing by its value in the unstructured chaotic regimes ($2\Delta_0$). When positive, π returns an overlap; when negative, it measures a distance between the two orbits. For every set of the architecture parameters, the theoretical expected value of the overlap can be computed within the DMF framework. We show that, in finite-size networks, the transition probability between the two chaotic attractors monotonically increases with the attractors overlap in the phase space. In the figure, the points returned by simulations are fitted with an error function of which we evaluate numerically the amplitude, the offsets and the gain: $f(x) = p_0 + p_1 \operatorname{erf}(p_2(x - p_3))$. Choice of the parameters: $\rho = 0$, $g = 3.0$, $\Sigma_m = 0$.

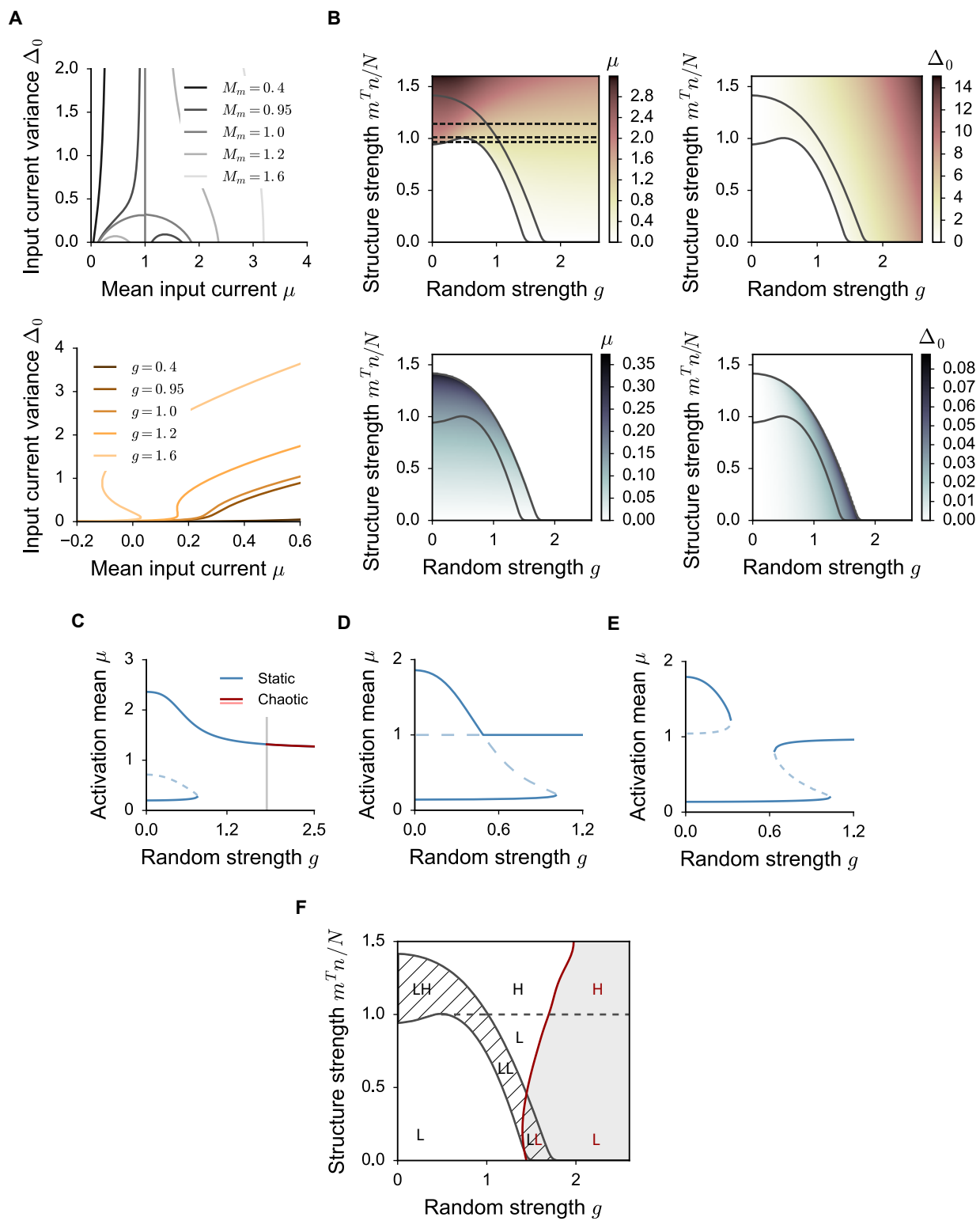


Figure S7 (*previous page*): **Dynamics of unit-rank networks with positively-defined activation functions.** Related to Figure 1.

In the main text, we performed our analysis of low-rank networks by adopting a completely symmetric network model, whose input-free solutions are invariant under the sign transformation $x_i(t) \rightarrow -x_i(t)$. Such symmetry is broken when a more biologically-plausible, positively-defined activation function $\phi(x)$ is adopted. Here, we investigate the effect of changing the transfer function to: $\phi(x) = 1 + \tanh(c(x - \gamma))$. Note that adding a shift γ is equivalent to including an external and constant negative input. The parameter c , instead, rescales the slope of $\phi(x)$ at the inflection point. For simplicity, we fix $\gamma = 1$ and $c = 1.5$. We furthermore restrict the analysis to the case of unit-rank structures whose right- and left-connectivity vectors solely overlap on the unitary direction ($\rho = 0$, see *Methods*). The Dynamical Mean Field (DMF) sets of equations were derived for an arbitrary activation function, so they can directly be adapted to the present scenario. **A.** We start by graphically analysing the stationary solutions (Eq. 83), and we plot the two nullclines of the system for different values of the architecture parameters. The top panel displays the μ nullclines for different $M_m M_n$ values. At $M_m M_n = 1$, the unstable branch coincides with $\mu = 1$, and the stable ones are symmetric. Around $M_m M_n = 1$, the perfect pitchfork is broken in one or the other direction, generating a first stable continuous branch and a second one, where one unstable and one stable solution merge at low or high firing rate. For extremely low (resp. high) $M_m M_n$ values, finally, there's just one nullcline at low (resp. high) μ values. The Δ_0 nullcline (bottom panel) displays a more complex behaviour compared to the symmetric $\phi(x) = \tanh(x)$ case. When g is sufficiently large, indeed, it can become a non-monotonic function of the mean input μ , transforming into a S -shaped nullcline. As it is shown in the following, this more complex shape is able to induce bistable activity even when the μ nullcline is reduced to a single continuous branch. This situation is reminiscent of the *fluctuations driven* bistable regime in [Renart et al, 2007]. **B.** Stationary stable solutions plotted as color maps on the parameter space defined by the random and the structure strengths. The mean-field system admits two classes of stable solutions. The first one, illustrated in the top row, takes large mean and variance values. It suddenly disappears on the leftmost grey boundary of the plot, in a parameter region which co-exists with the second solution. The second solution, plotted in the bottom row, takes typically small values of μ and Δ_0 , and disappears on the right-most boundary with a first-order transition as well. **C-D-E.** In order to dissect more systematically the nature of those solutions, we fix the value of the structure strength (dashed lines in in B), and we gradually increase the random strength g . In **C**, we fix the structure strength to high values: $M_m M_n = 1.2$. The bifurcation pattern occurring in this case resembles what we observed in the original case with $\phi(x) = \tanh(x)$. At low values of g , two stable fixed points are built, respectively, on the high and on the low branches of the μ nullcline. For that reason, we call this state LH (cfr with F). When the random connectivity is too strong, the low firing rate fixed point annihilates, and only one high firing solution survives (H state). In **D**, $M_m M_n$ is exactly equal to unity. At small g values, similarly to the previous case, network activity is bistable and admits one L and one H stationary state. As g increases, the Δ_0 intersect the high firing rate branch at smaller and smaller values of μ . Finally, the H state is lost, and the second stable fixed point is realized on the intermediate branch at $\mu = 1$. This bistable state is thus formally a LI state. Finally, at large g values, the two intersections on the low rate branch collapse together and disappear. Bistability is lost and only one intermediate (I) state exists. In **E**, we consider slightly smaller values of $M_m M_n$. A classical LH state exists at small g values, the bistable state at large random strengths involves two stable solutions which originate both a low firing rates (LL state). The two states strongly differ in the value of their variance. When g is sufficiently large, one unique low firing rate, high variance state (L) survives. **F.** The different activity states are finally sketched in the phase diagram. Note that I states separate the phase diagram in F in two macro areas: below the dashed line, every stationary and chaotic solution is built on the same low firing rate branch of the μ nullcline, and is thus formally a L state. Finally, the exact shape of the phase diagram depends on the value of the parameters c and γ . Choice of the parameters: $\rho = 0$, $\Sigma_m = 0$.

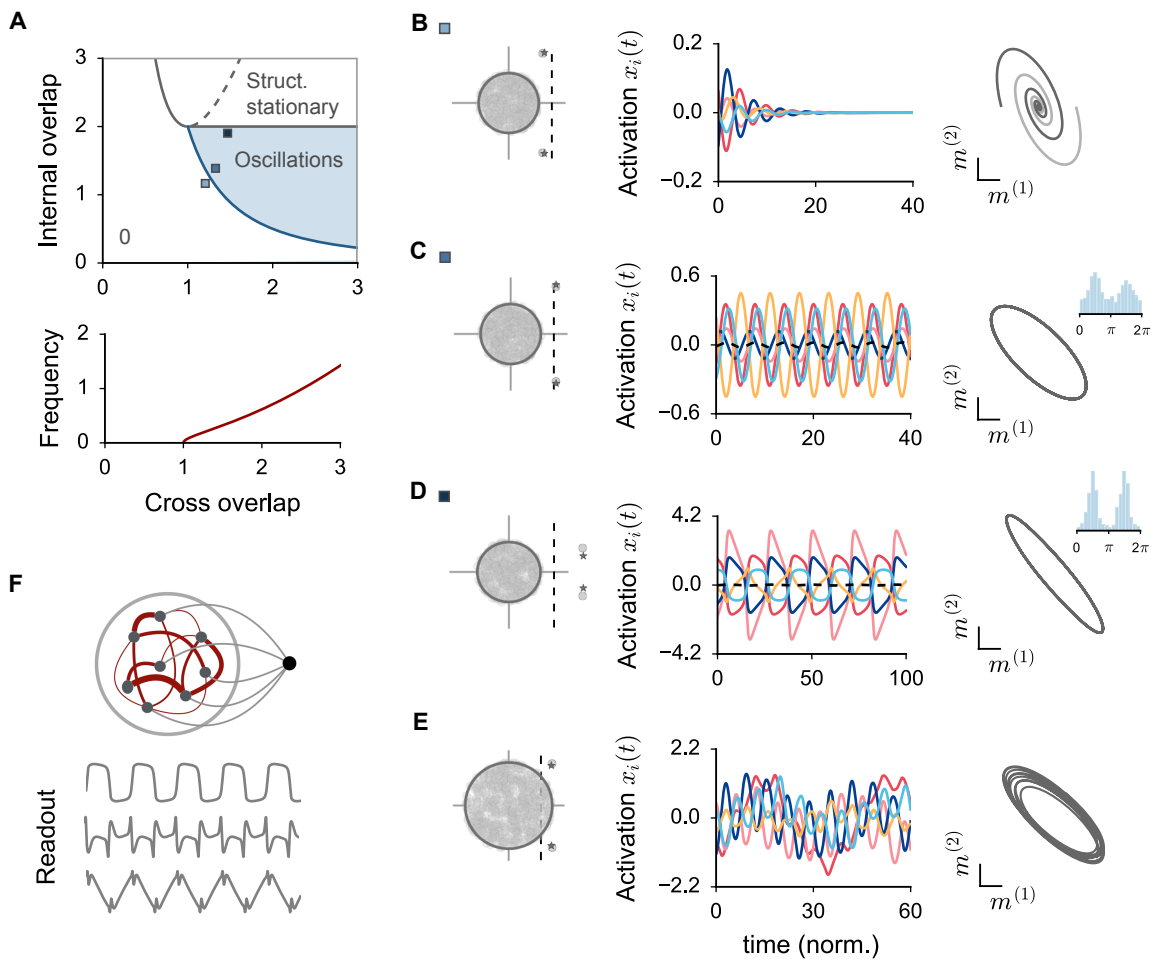


Figure S8 (*previous page*): **Oscillatory activity from rank-two structures that include a cross overlap between left- and right-connectivity vectors.**

A. Top: phase diagram for the rank-two structure with negative cross-overlap (see *Methods*). For different values of the internal and the cross overlaps, the trivial fixed point can lose stability and give rise to oscillatory or stationary structured activity. The Hopf bifurcation is indicated in blue, the instability to stationary activity in grey. The light-blue parameter region corresponds to sustained non-linear oscillations. Bottom: frequency of oscillations along the Hopf bifurcation boundary, in units defined by the implicit time scale of the network dynamics. **B-C-D-E.** Samples of activity for different connectivity parameters. From left to right: stability eigenspectrum of the trivial fixed point (theory and simulations), sample of activation trajectories (the population average is indicated in dashed black), and population dynamics obtained by projecting the population activation x on the right-connectivity vectors $m^{(1)}$ and $m^{(2)}$. The parameters that have been used for every sample are indicated in **A**. **B:** Oscillatory transients in the fixed point regime. **C:** Stable oscillations above the Hopf instability. The elongated shape of the closed trajectory on the $m^{(1)} - m^{(2)}$ plane is inherited by the phase distribution across the population, and can be tuned by slightly modifying the parameters of the rank-two structure (see *Methods*). **D:** Highly non-linear oscillations close to the boundary with bistable activity. **E:** Oscillatory activity at high g values ($g = 1.35$), where dynamics include a chaotic component. **F.** When oscillations are strongly non-linear, their spectrum includes a large variety of frequencies that can be used to reproduce highly non-linear periodic patterns. We designed three random readout vectors and we linearly decoded activity from the dynamical regime in **D** to generate periodic non-linear outputs, which are displayed in grey.